Astronomical Techniques and Instruments, Vol. 1, March 2024, 117–127

Article Open Access

An improved non-uniform fast Fourier transform method for radio imaging of coronal mass ejections

Weidan Zhang[1], Bing Wang[1], Zhao Wu[1], Shuwang Chang[1,3], Yao Chen[1,2], Fabao Yan[1,3*]

[1]*Laboratory for Electromagnetic Detection*, *Institute of Space Sciences*, *Shandong University*, *Weihai*, *Weihai* 264209, *China*

[2]*Center for Integrated Research on Space Science*, *Astronomy*, *and Physics*, *Institute of Frontier and Interdisciplinary Science*, *Shandong University*, *Qingdao*, *Qingdao* 266237, *China*

[3]*School of Mechanical*, *Electrical & Information Engineering*, *Shandong University*, *Weihai*, *Weihai* 264209, *China*

*Correspondence: yanfabao2022@163.com

Received: November 29, 2023; Accepted: December 22, 2023; Published Online: January 6, 2024; https://doi.org/10.61977/ati2024006

Citation: Zhang, W. D., Wang, B., Wu, Z., et al. 2024. An improved non-uniform fast Fourier transform method for radio imaging of coronal mass ejections. *Astronomical Techniques and Instruments*, **1**(2): 117−127. https://doi.org/10.61977/ati2024006.

Abstract: Radioheliographs can obtain solar images at high temporal and spatial resolution, with a high dynamic range. These are among the most important instruments for studying solar radio bursts, understanding solar eruption events, and conducting space weather forecasting. This study aims to explore the effective use of radioheliographs for solar observations, specifically for imaging coronal mass ejections (CME), to track their evolution and provide space weather warnings. We have developed an imaging simulation program based on the principle of aperture synthesis imaging, covering the entire data processing flow from antenna configuration to dirty map generation. For grid processing, we propose an improved non-uniform fast Fourier transform (NUFFT) method to provide superior image quality. Using simulated imaging of radio coronal mass ejections, we provide practical recommendations for the performance of radioheliographs. This study provides important support for the validation and calibration of radioheliograph data processing, and is expected to profoundly enhance our understanding of solar activities.

Keywords: Radio interference; Gridding; Imaging; Non-uniform fast Fourier transform

1. INTRODUCTION

CMEs refer to the rapid large-scale ejection of magnetized plasma from the solar corona[1-4]. When high-energy particles released by CMEs reach the Earth, they can potentially damage satellites and impact communication networks and power grids [5-7] . Studying their propagation process, detecting and tracking them, and observing how high-energy particles propagate in space are of great significance in the accurate prediction of space weather[8] to preempt and mitigate any disruption. Radioheliographs, as conventional equipment for solar radio observations, can monitor CMEs and other solar eruptive activities[9,10].

Radioheliographs, based on the principle of aperture synthesis imaging, use antenna arrays to receive solar signals. By cross-correlating every pair of received signals, a Fourier component of the source is obtained, and the visibilities can be determined by combining multiple components. These visibilities undergo a Fourier inverse transform to obtain the sky brightness distribution, known as the "dirty map", $I^D(l,m)$[11].

$$I^D(l,m) = \iint V(u,v)S(u,v)\mathrm{e}^{-2\pi\mathrm{i}(ul+vm)}\mathrm{d}u\mathrm{d}v\ . \qquad (1)$$

Solar radio observations provide images with high spatial resolution, and are among the most effective means for observing and studying CMEs. On April 20, 1998, a very interesting CME event was observed by the Nancay radio heliograph[12] (NRH) in France. This was the first direct imaging of an expanding CME halo in the radio frequency range, which was found to be very similar to the corona observed by the large angle spectroscopic coronagraph (LASCO) and became known as a "radio" CME[13].

Radio observations have high temporal resolution and can be conducted at multiple frequency points, allowing for better tracking of the evolution of CMEs[14]. With radio imaging, there is no need for an occulting disk.

Under favorable observing conditions, the process of CME lift-off and the gradual expansion of the CME halo can be clearly observed[15,16]. However, due to the short duration of CME events, it is challenging to perform radio imaging of CMEs[17], particularly in the early stages of their eruptions. So far, only a few observations have obtained radio images of CMEs[13,18,19].

NRH[12], Nobeyama radioheliograph[20] (NoRH) in Japan, Siberian solar radio telescope[21] (SSRT) in Russia, and other radioheliographs have observed solar flares and eruptive events in their respective frequency ranges, providing an important observational foundation for studying flares and CMEs. In recent years, a new generation of advanced radio telescope facilities capable of solar observations have been developed, such as the low-frequency array[22] (LOFAR), Murchison widefield array[23], Mingantu ultrawide spectral radioheliograph[23,24], and Square Kilometer Array[25] (SKA), which can provide good spatial-frequency resolution for solar imaging. Additionally, the recently constructed Daocheng solar radio telescope (DSRT) in Daocheng, China, can observe CMEs with high dynamic range and sensitivity in the frequency range of 150−450 MHz[26,27]. Routine imaging observations of radio CMEs contribute to the understanding of magnetic fields within active regions and CMEs, providing powerful diagnostic data for solar physics research.

Imaging simulations are of significant importance both before and after the construction of the equipment. These can provide references for designing the performance parameters of the equipment while also helping to understand the performance of existing instruments, and verifying parameters and imaging capabilities.

The utility of imaging simulations is demonstrated by, for example, the Brazilian decimetric array[28] (BDA). To analyze its imaging capability, the BDA simulated solar radio models at 1.5 GHz and compared them with radio images acquired by the NoRH at 17 GHz[29]. NoRH evaluated the 17 GHz images, analyzing the closure relationships and causes of baseline errors. In snapshot mode simulation analysis, the imaging results were assessed with the presence of baseline errors in the visibility, and the dynamic range of the images was calculated.

Simulations and modeling play a crucial role in the design and evaluation of radio interferometric observations[30]. Currently, widely used imaging software packages include Common Astronomy Software Applications[31] (CASA), Astronomical Image Processing System[32] (AIPS), and Difmap[33]. These packages primarily cater to the data processing needs of radio telescopes such as Atacama Large Millimeter/submillimeter Array[34] (ALMA) and Very Large Array[35] (VLA). As solar radio telescopes continue to evolve and new types of radio telescopes become established, there is a need for imaging simulation software that is suitable for different radio facilities. Furthermore, existing simulation software often adopts simplified assumptions to reduce computational requirements, sacrificing accuracy for speed. This may result in unexpected numerical effects that are difficult to distinguish from real effects observed in the data.

To provide reference for the design and optimization of radioheliographs, this work proposes an imaging simulation pipeline, which performs the entire process from antenna configuration, UV distribution calculation, visibility sampling, weighting, gridding, and fast Fourier transform (FFT) to obtaining the dirty image. It also provides various algorithms for different heliograph imaging needs, and performs imaging simulations of point source, surface source, and radio CME models in snapshot mode. The following sections will mainly introduce the imaging simulation pipeline. Section 3 provides a detailed description of the imaging simulation experiments. Section 4 discusses and analyzes the imaging results under different scenarios of radio CME models, and the conclusion summarizes the results.

2. IMAGING SIMULATION PIPELINE

The proposed radioheliograph imaging simulation pipeline in this paper can meet various needs of solar observations. Currently, it can achieve the following functions:

(1) Antenna configuration design.

(2) Calculation of coordinates of uv-axis (UV) and baselines.

(3) Visibility simulation based on given source structure (sky model) and antenna positions.

(4) Calculation of dirty image and point spread function (PSF), providing quality evaluation for observations at a given configuration.

2.1. Imaging Steps

The simulation process is illustrated in Fig. 1, and the specific steps are as follows:

(1) Construction of the antenna array, with antenna positions set in the local Cartesian coordinates coordinate system (ENU) with the unit in meters. The antennas are positioned in the same plane, with their normal vector pointing toward the zenith direction at the observation site.

(2) Coordinate transformation. Calculation of solar right ascension, declination, and hour angle for specified observation times, and computation of the coordinate transformation matrix from the ENU coordinate system to the UVW coordinate system.

(3) Visibility calculation. Assuming the solar center corresponds to the phase center and the coordinate system corresponds to the sky plane coordinate system, numerical values of the UV plane sampling points are calculated based on the sky model. This step obtains the visibility values. It is important to consider the occlusion caused by antenna projections when calculating the UV sampling points, and select the UV plane projection as the sampling point for calculation at the specified moment.

(4) Gridding the sampling points. Application of interpolation, a convolution gridding method, or improved NUFFT to grid the non-uniformly sampled visibility. In this step, the grid method can be chosen based on the

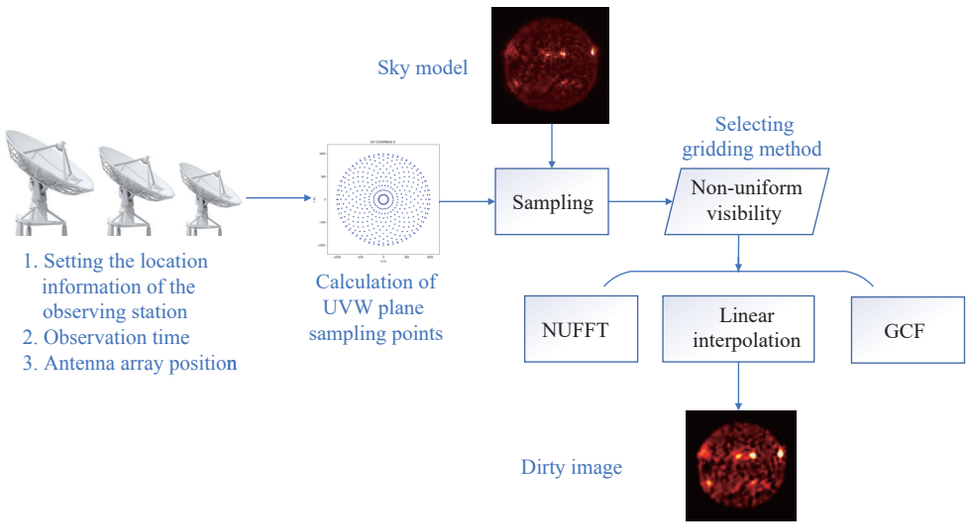

Fig. 1. Process of the imaging simulation pipeline.

actual antenna configuration and other factors.

(5) Image reconstruction. There are two available methods: One method is to perform FFT on the visibility to obtain the dirty image, while the other is to apply direct Fourier transform using the UV points for image reconstruction. The following sections will provide detailed explanations of these methods.

2.2. Imaging Algorithms

There are two methods available for imaging simulation: The direct Fourier transform method and the FFT method. Within the gridding algorithm, there are three options to choose from: Linear interpolation, convolved gridding function, and improved NUFFT method.

The direct Fourier transform method directly performs Fourier transformation on the visibility function based on the principles of synthesis imaging, which yields the dirty image, as

$$I(l,m) = \sum V(u_i, v_i) W_i \mathrm{e}^{2\pi \mathrm{i}(lu_i + mv_i)} , \qquad (2)$$

obtaining the image by summing and computing all the UV sampling points. The weighting function, W_i, is calculated based on the corresponding surface element for each sampling point, and the resulting visibility is numerically integrated to obtain the dirty image. This method is the conventional approach for radioheliograph imaging.

When there is an increasing number of baselines and integration time, the computation time using the direct Fourier transform method can significantly increase. Therefore, the FFT method is commonly used for efficiency. To leverage the computational efficiency of FFT for rapid image reconstruction, the visibility needs to be allocated onto a regular grid, in a process known as gridding. Our simulation pipeline provides three interpolation methods, with linear interpolation being the simplest approach for grid construction. This method does not require weighting operations, reducing computational load and resulting in shorter image reconstruction time.

The goal of linear interpolation gridding is to create a regular data grid, onto which irregularly sampled data points can be interpolated. This is achieved by estimating the values at positions between two data points using the linear relationship between neighboring data points. Typically, the values of grid points are estimated by taking a weighted average of neighboring data points, which simplifies the grid generation process and saves computational time, as no additional weighting calculations are required.

The convolution gridding method is used in the data processing of imaging to grid the unevenly distributed visibility function data using a convolution gridding function, resulting in uniform UV sampling data. Commonly used convolution gridding functions include square wave function, sinc function, Gaussian sinc function, and elliptical basis function. As convolution operations are involved, the computation time for this method is comparatively longer.

To further address the issue of unevenly distributed UV sampling points, this work proposes an improved NUFFT method. This method uses an efficient algorithm designed for the computation of a one-dimensional "type 1" NUFFT. The principle behind the algorithm is given by

$$f_k = \sum_{j=1}^{M} c_j \mathrm{e}^{\mathrm{i}kx_j} , \qquad (3)$$

where M is a set of real sample points $x_j \in [0, 2\pi]$, corresponding complex coefficients c_j for $(j = 1, \cdots, M)$, and a requested integer number of modes N, the goal of the NUFFT is to efficiently compute the Fourier series coefficients f_k where k ranges over the integer interval $-N/2 \leqslant k \leqslant N/2 - 1$.

Traditional direct computation of this series would require $O(NM)$ operations, but the improved NUFFT employs a sequence of optimized steps, including spreading, FFT, and deconvolution, to approximate the vector of answers within the user-specified relative tolerance. The

overall computational complexity is $O(N\log N+M)$, almost linear with respect to N and M. This speed-up is analogous to that achieved by the FFT.

The improved NUFFT boasts several key features, including the incorporation of a groundbreaking "exponential of semicircle" kernel[36]. Additionally, it employs numerical approximations for the Fourier transform of this kernel, load-balanced multithreaded spreading and interpolation, point sorting to enhance cache reuse, and a low upsampling option tailored for smaller FFTs, especially in type 3 transforms.

In terms of memory efficiency, the algorithm avoids precomputation, always evaluating the kernel on the fly. This results in a memory footprint often an order of magnitude less than the fastest precomputed modes of competitors, such as non-uniform fast Fourier transform 3 (NFFT3) and the Michigan Image Reconstruction Toolbox (MIRT), especially at high accuracy.

An advantage of our algorithm is its automated kernel parameter selection. Unlike some alternatives, users are not required to concern themselves with kernel choice or parameters. Instead, the user simply specifies the desired relative accuracy, and NUFFT parameters are automatically selected to achieve this accuracy as efficiently as possible.

The steps are as follows: First, the sampled visibility function is weighted. Then, the non-uniformly sampled data are divided into different regions, and interpolation techniques are used to approximate them as uniformly sampled data. Finally, the discrete Fourier transform (DFT) is computed using the FFT algorithm on these uniformly spaced data. The resulting DFT is then mapped back to the original non-uniform positions using interpolation, yielding the dirty image. This improved NUFFT method optimizes both computational efficiency and accuracy.

In general, the conventional direct Fourier transform algorithm is capable of inverting the imaging process with good accuracy. However, due to the large number of antennas in radioheliographs, it has the longest computation time. The gridding algorithm, when using the convolution gridding method, may result in lower inversion accuracy and introduce artifacts, but it has lower computational complexity, leading to faster computation speed. The improved NUFFT algorithm provides higher inversion accuracy and is suitable for imaging with arbitrary and irregular frequency distributions. However, the drawback of NUFFT is its high computational complexity, requiring more computation time. Therefore, when conducting imaging simulations, the choice of algorithm should be based on the specific scenario. The following sections will provide detailed comparative analysis of imaging simulations using these algorithms.

3. IMAGING SIMULATION EXPERIMENTS

The Sun, as the target source, has the characteristic of being an extended source. The solar radio flux is relatively strong and has the characteristic of instantaneous changes. Therefore, this study adopts a snapshot approach in the simulation. In the simulation, the observing frequency is set at 300 MHz, with the solar center as the phase center, a field of view of 3° × 3°, and cell size of 103". The interferometric array used is a 313-unit uniform circular array with a diameter of 1 000 m[25]. The antenna configuration and UV coverage at 12:00 on the summer solstice are shown in Fig. 2.

3.1. Construction of the Sky Model

In this study, the following three radio sources are selected as the sky model. The image size is set as 128 × 128 pixels, with each pixel representing 42.1875 × 42.1875 arcsec.

(1) Gaussian point source. A Gaussian distribution source is placed in the image, with a peak brightness temperature of 1.24×10^6 K, as shown in Fig. 3A.

(2) Surface source with active regions. Solar images are obtained using AIA304 data and normalized. The

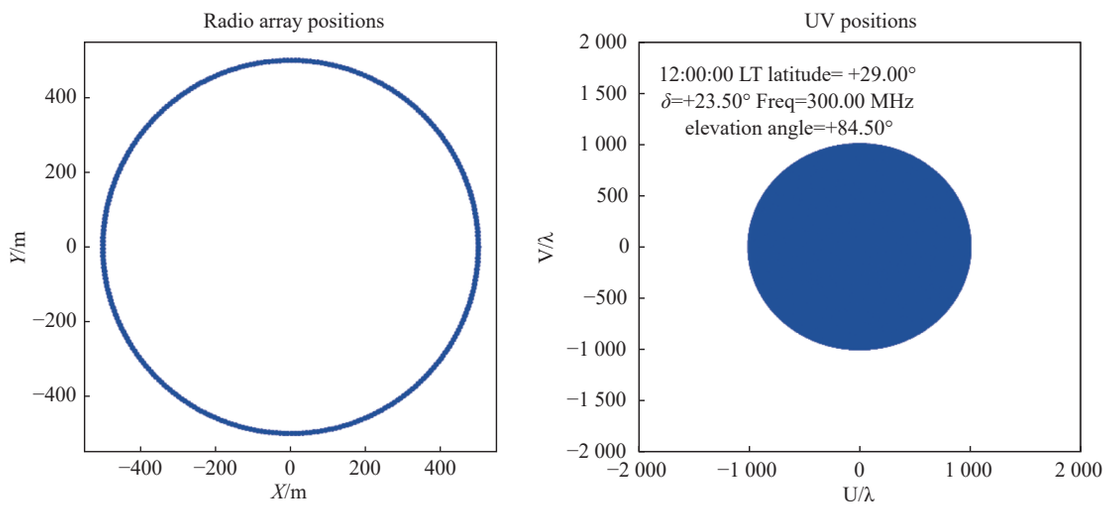

Fig. 2. Antenna positions and UV coverage at summer solstice and noon.

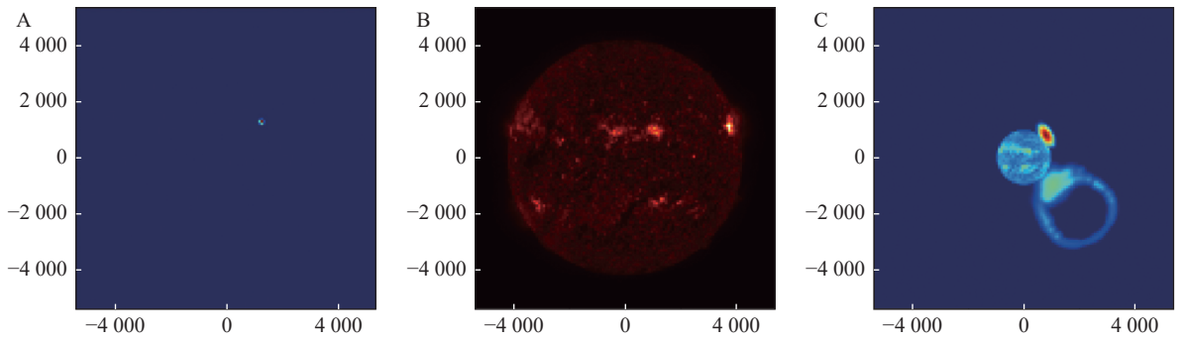

Fig. 3. Sky models of three types of radio sources used for simulation. (A) Gaussian point source. (B) Surface source with active regions. (C) Radio CME Model.

peak brightness temperature is set to 1.24×10^6 K, as shown in Fig. 3B.

(3) Radio CME Model. Currently, there are two well-observed radio CME events. On April 20, 1998, an expanding CME ring was directly imaged in the radio band, which was very similar to the coronal image observed by LASCO[13]. The outer ring had a maximum brightness temperature of 2×10^4 K, and the inner ring had a brightness temperature of 5.6×10^5 K, as shown in Fig. 3C. Furthermore, on April 15, 2001, NRH observed another radio CME event, which showed good correlation with the high-energy electron events observed by the electron, proton, and alpha-particle monitor (EPAM) experiment on the advanced composition explorer (ACE) spacecraft[17]. In this event, the position angle of the white-light CME was approximately same as that of the radio ring, with similar morphology and expansion.

On the basis of these two events, we can summarize the following observation characteristics of radio CMEs:

(1) They exhibit a loop-like structure similar to the white-light coronagraph morphology (possibly dependent on the viewing angle), with a observed range greater than $2\ R_\odot$.

(2) They generally occur in association with type-IV radio storms, often accompanied by type-II and type-III radio bursts.

(3) The brightness of the ring area is similar to the background radiation, with stronger radio sources near the solar disk.

(4) They exhibit similar evolution characteristics to white-light CMEs.

Based on these characteristics, this study constructs a radio CME model to simulate imaging as part of the sky model. The specific settings are as follows:

(1) Solar disk. With active regions and peak brightness of 1×10^5 K.

(2) Noise storm. Set as a Gaussian source with a peak brightness of 1×10^8 K.

(3) CME. Set as a Gaussian point source with peak brightness at the CME base of 5.6×10^5 K and at the top of 2×10^4 K.

(4) Sky background. Brightness temperature of 1×10^2 K (illustrated in Fig. 3C).

3.2. Evaluation of Imaging Quality

The simulation results of the three algorithms for different radio sources are shown in Fig. 4. To visually analyze the imaging performance of several dirty images, this work employs the profile slicing method to compare the simulated dirty images with the sky model. For Gaussian point sources and extended sources with active regions, a slanted slice at $y = x$ is selected for comparison. For extended sources, the focus is on comparing the imaging of faint sources, so an elliptical slice is chosen. The comparison results are shown in Fig. 5. Through comparison, we find that all three algorithms exhibit good imaging performance for different radio sources, effectively displaying the contours and details of the sky model. However, due to the sparse sampling of the sky model currently, there is a certain level of error between the dirty images and the sky model, preventing them from being completely identical.

This work quantitatively measures the quality of images from two aspects: Dynamic range and fidelity. Dynamic range is typically defined as the ratio of peak radiation intensity in the image to the standard deviation of image noise, while fidelity is defined as the difference between the standard model divided by the difference between the standard model and the recovered image[37], given by

$$\text{fidelity} = \sum_{i,j} \frac{|m(i,j)|}{|m(i,j) - r(i,j)|}, \tag{4}$$

where $m(i,j)$ represents the standard model and $r(i,j)$ represents the recovered image. Since the denominator in the above equation may be zero, to avoid extreme situations, we redefine the fidelity by taking $diff = m(i,j) - r(i,j)$, The updated definition of fidelity is thus given by

$$\text{fidelity} = \sum_{i,j} \frac{|m(i,j)|}{\max\left[|diff(i,j)|, 0.7\,\text{rms}(|diff(i,j)|)\right]}. \tag{5}$$

We find that under the same conditions, the three algorithms exhibit a high dynamic range for different radio sources in the simulated images of the uniformly distributed circular array, ranging from a minimum of 30.77 dB to over 40 dB, as shown in Tables 1. This not only confirms the effectiveness of the imaging algorithms but

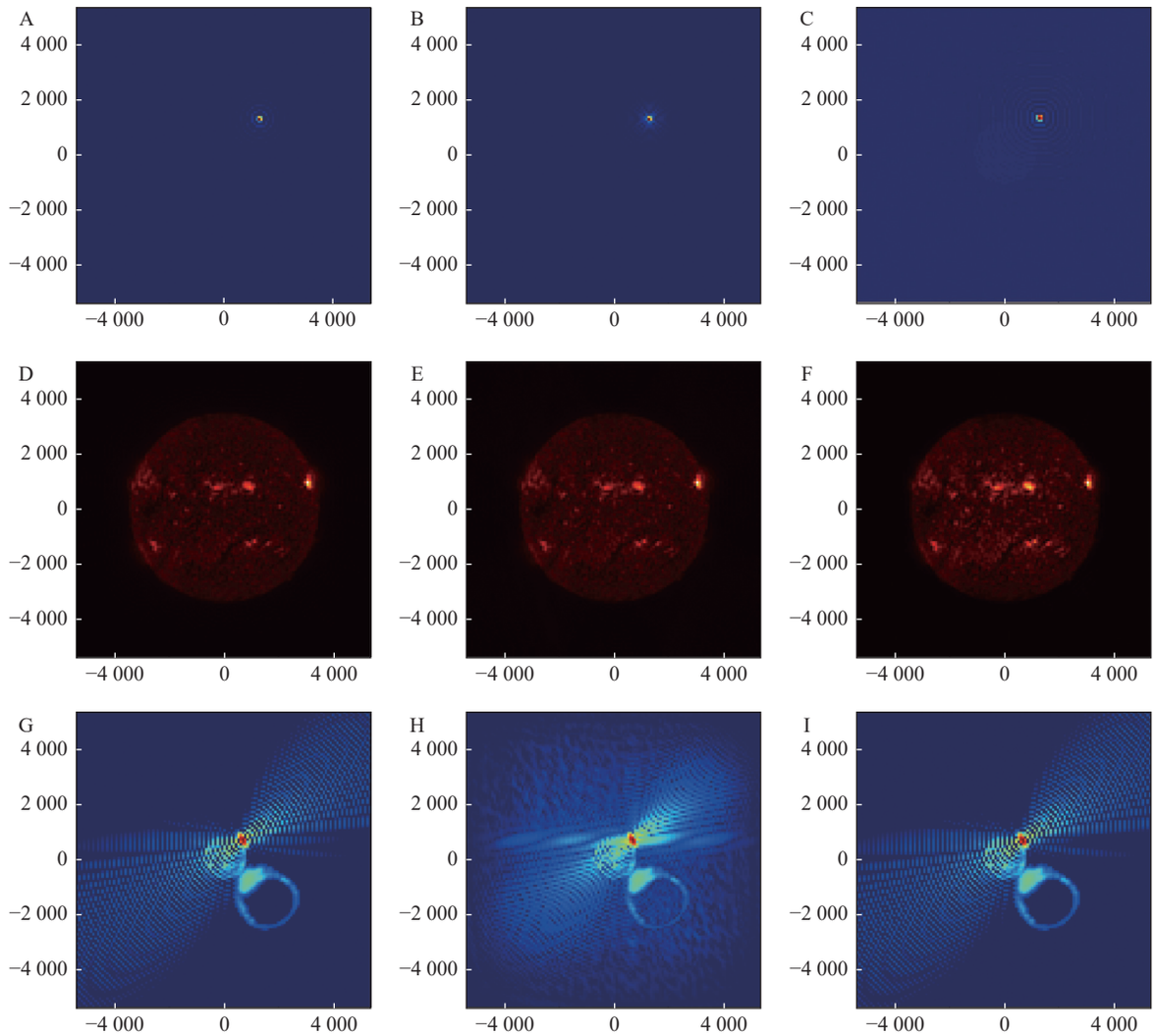

Fig. 4. Subplots A−C show the imaging results of the Gaussian point source using three algorithms. From left to right, the imaging methods employed are direct Fourier transform numerical integration, NUFFT algorithm, and FFT algorithm. Subplots D−F show the imaging results of the surface source with active regions using three algorithms. Subplots G−I show the imaging results of the radio CME model using three algorithms.

also demonstrates the imaging capability of the uniformly distributed circular array. Comparing the three algorithms, the imaging fidelity is highest for the direct Fourier transform numerical integration method, but this also requires a longer computation time. The method based on FFT with linear interpolation, using natural weights, has the shortest computation time but introduces more noise interference, requiring further deconvolution operations. The improved NUFFT method provides a compromise between computation time and resulting image quality. For the uniformly distributed circular array, the improved NUFFT algorithm is a preferable choice among the three algorithms.

3.3. Comparison with the NIFTY-gridder Algorithm

NUFFT has been widely used in radio interferometer imaging. To further illustrate its performance, we analyze the algorithm proposed in this paper in comparison with the NIFTY-gridder algorithm[38] used by the SKA. Here, we do not consider a wide field of view, and the algorithm is required to have an error that is less than 2×10^{-13}. Additionally, both algorithms are used to map the radio CME model without GPU acceleration. The results are shown in Fig. 6 and Table 2.

The imaging results obtained by the two methods, compared in Fig. 6 and Table 2, exhibit minimal differences. The improved NUFFT algorithm has a higher dynamic range of imaging compared with the NIFTY-gridder algorithm, while the NIFTY-gridder algorithm demonstrates faster data processing capabilities. This is mainly because high-performance distributed parallel computing is employed to use the NIFTY-gridder algorithm, giving enhanced computational performance, and this advantage is particularly pronounced in multi-channel calculations. This simulation employs single-frequency channel imaging, enhancing the effectiveness of the improved NUFFT algorithm.

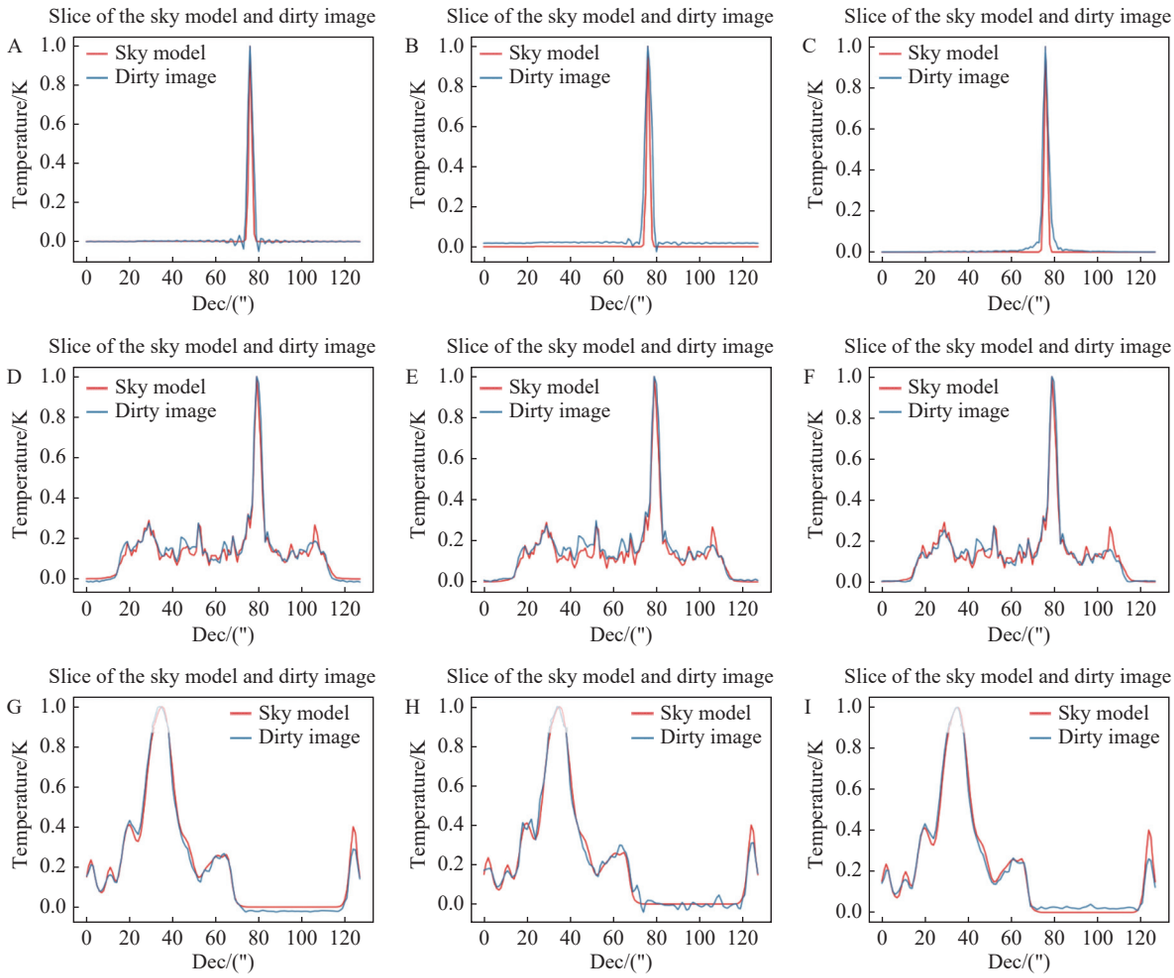

Fig. 5. A comparative profile plot of imaging results using three algorithms for different radio sources. From left to right, the imaging methods employed are direct Fourier transform numerical integration, NUFFT algorithm, and FFT algorithm. Subplots A−C show the comparative plot of three algorithms for a Gaussian point source, subplots D−F present the comparative plot for a surface source with active regions, and subplots G−I display the comparative plot for the radio CME model.

Table 1. Comparison of imaging results of three algorithms for Gaussian point sources, surface sources, and the radio CME model

	Parameters	DFT (linear interpolation)	FFT (linear interpolation)	NUFFT
Gaussian point sources	Image fidelity	218	156	156
	Time/s	35	3	21
	Dynamic range/dB	36	35	38
Surface sources	Image fidelity	26 174	5974	5974
	Time/s	36	2	22
	Dynamic range/dB	33	30	36
The radio CME model	Image fidelity	168	161	161
	Time/s	35	2	22
	Dynamic range/dB	41	37	44

4. DISCUSSION

Section 3 has provided the imaging results and analysis of the uniformly distributed circular array for radio CMEs. However, to further investigate the conditions under which the radioheliograph can achieve comparatively good imaging of radio CMEs, considering the comprehensive evaluation of the previous comparison results, the improved NUFFT algorithm is used to discuss the radio CME radiation model in four different scenarios.

In the first scenario, the peak intensity of the noise storm is set to 1×10^8 K, and its contrast ratio with the weakest part of the radio CME is 40 dB. The CME ring is not within the influence range of the noise storm sidelobes, as shown in Fig. 7A. The CME ring can be clearly seen in Fig. 8A, and the sidelobe effects of the noise

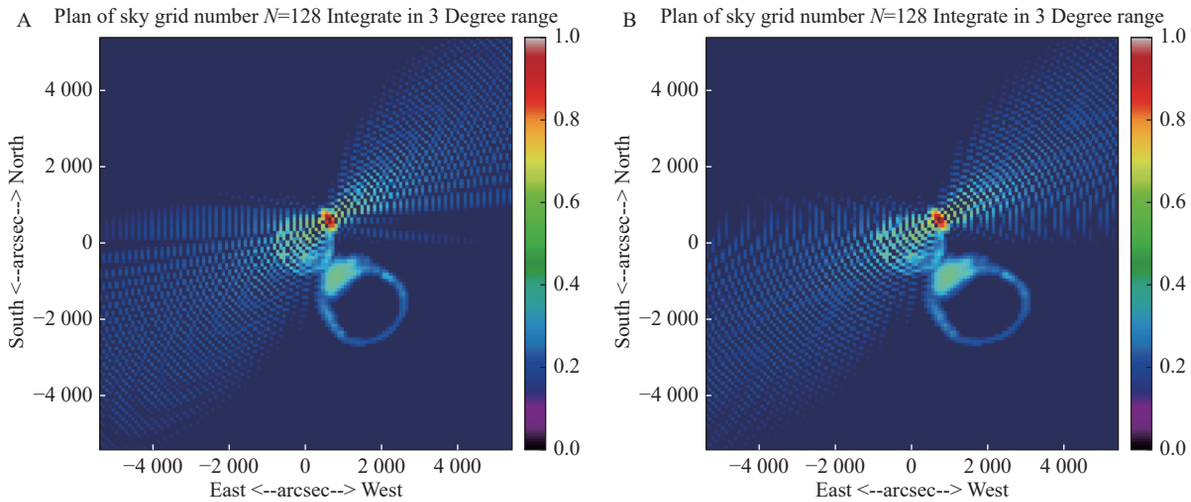

Fig. 6. Comparison of two algorithms for dirty maps. (A) The result of NUFFT algorithm. (B) The result of NIFTY-gridder algorithm.

Table 2. Comparison of imaging results of two algorithms for the radio CME model

Parameters	NIFTY-gridder	NUFFT
Image fidelity	161	161
Time/s	20	22
Dynamic range/dB	41	44

storm are also evident. Since the position of the CME ring is outside the sidelobe influence range of the noise storm, the CME ring can be observed clearly.

For the second scenario, the peak intensity of the noise storm is set to 1×10^7 K, and its contrast ratio with the weakest part of the radio CME is 30 dB. The CME ring is not within the influence range of the noise storm

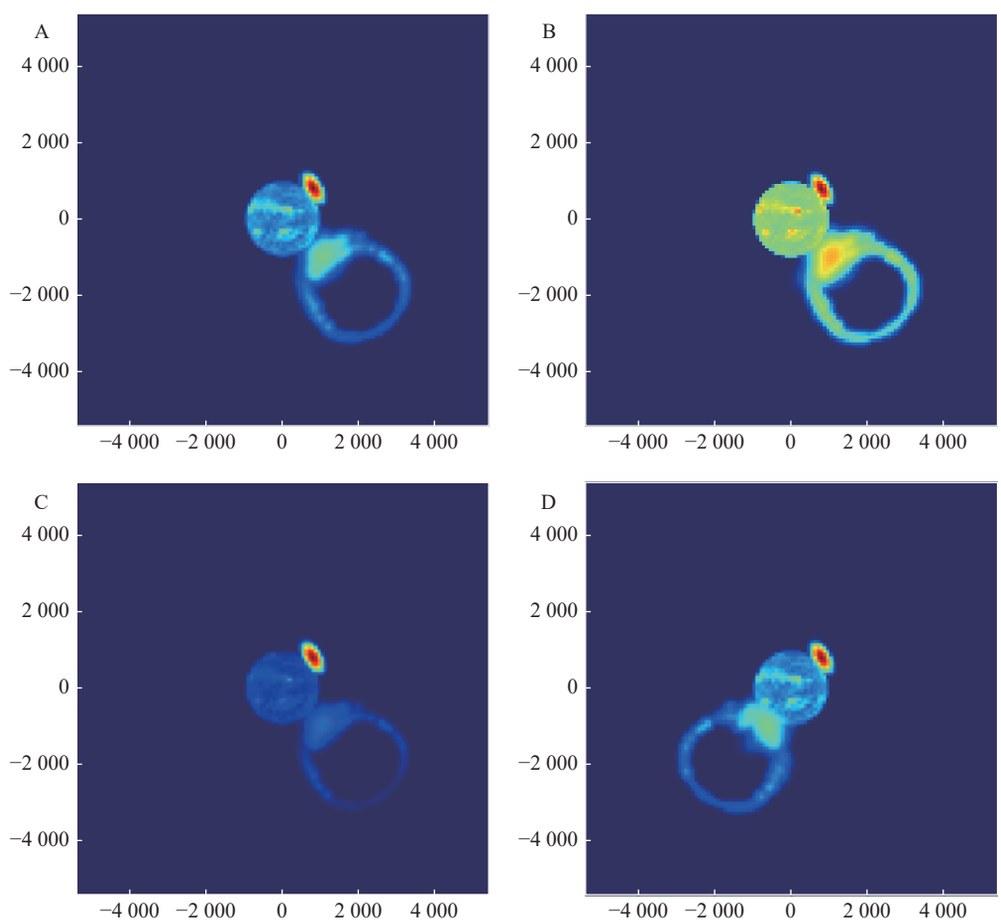

Fig. 7. Four scenarios of radio CME.

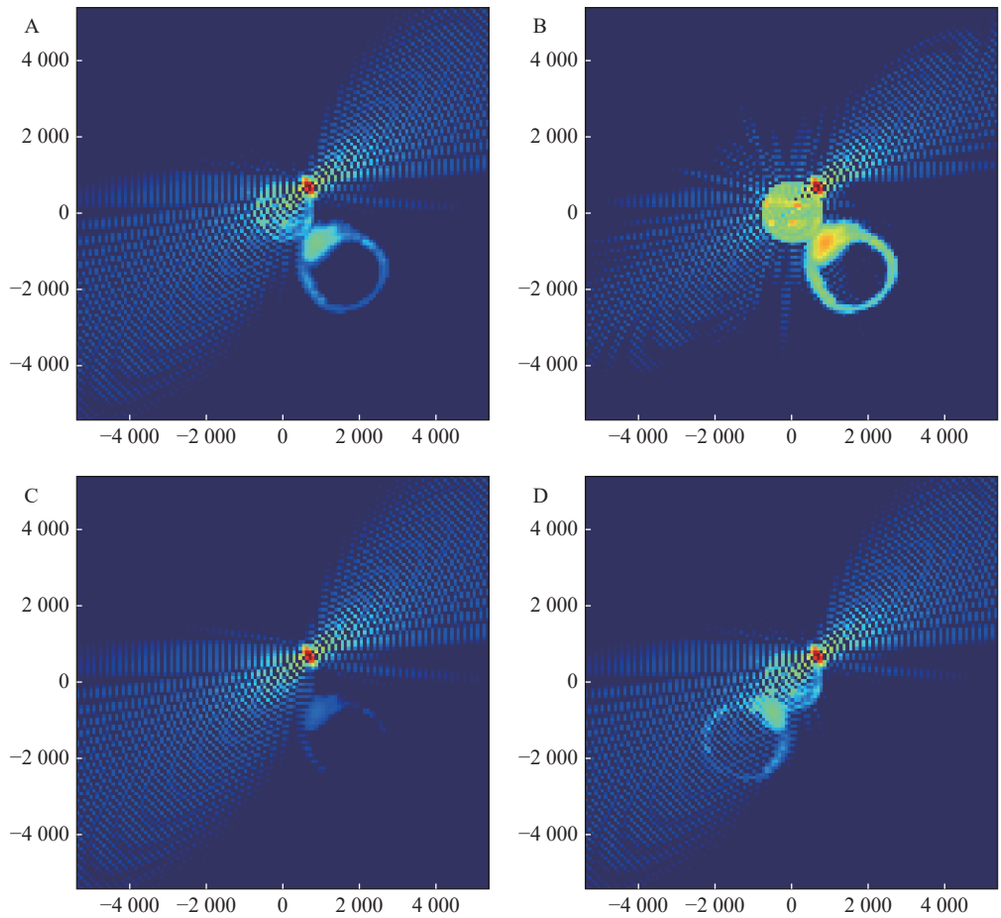

Fig. 8. Imaging results for different models of radio CME.

sidelobes, as shown in Fig. 7B. Since the peak intensity of the noise storm is reduced, its impact on the faint sources is smaller. Therefore, in the image, the CME ring can be seen more clearly (Fig. 8B).

In the third scenario, the peak intensity of the noise storm is set to 1×10^9 K, and its contrast ratio with the weakest part of the radio CME is 50 dB. The CME ring is not within the influence range of the noise storm sidelobes, as shown in Fig. 7C. In this case, the peak intensity of the noise storm is enhanced, and the complete radio CME ring cannot be observed in the image (shown in Fig. 8C). Only the base and the left and right branches are visible, while the weakest part cannot be seen. Therefore, when the intensity contrast between strong and weak sources reaches 50 dB, it is not possible to achieve a complete observation of the radio CME.

In the final scenario, the peak intensity of the noise storm is set to 1×10^8 K, and its contrast ratio with the weakest part of the radio CME is 40 dB. The CME ring is within the influence range of the noise storm sidelobes, as shown in Fig. 7D. In the image, the outline of the radio CME can be seen in Fig. 8D, but the details are affected by the sidelobes of the strong sources. Deconvolution operations are required to enhance the visibility of the image and to reveal the details clearly.

In summary, the ability of the uniformly distributed circular array to observe radio CME events, as well as the intensity contrast between strong and weak sources and the position of the CME ring, depends on the operational status of the instrument and the occurrence of the event during observation. When the intensity contrast between strong and weak sources is less than 40 dB and the position of the CME ring is not within the influence range of the sidelobes from strong sources, the uniformly distributed circular array can achieve a complete observation of the radio CME event.

5. CONCLUSION

CMEs are frequent solar eruption phenomena in the solar atmosphere. They are the largest and most spectacular solar events and the main driving source for hazardous space weather. Researches on CMEs have been conducted for several decades, mainly focused on observations in the visible wavelength range. However, phenomena corresponding to white-light CMEs have been rarely observed in the radio band. Radio observations have the advantages of high temporal resolution and multiple frequency bands, enabling better tracking of CME evolution. Imaging of radio CMEs allows observation of the early propagation process of CMEs without being affected by occulting disks, allowing more detailed study of the evolu-

tion process and inference of the magnetic field distribution of CMEs. Additionally, there is a good correspondence between low-frequency radio storms and CMEs in terms of size and latitude distribution[38]. Therefore, a high-sensitivity low-frequency array is an ideal choice for imaging radio CMEs.

This study evaluates the imaging performance of a radioheliograph on radio CMEs through a simulation pipeline, focusing on different radio sources. Our proposed improved NUFFT algorithms for gridding show excellent imaging results for various radio sources in snapshot mode, achieving good effects on both point and extended sources without the need for deconvolution processing. The dynamic range of the images surpasses 30 dB. A comparative analysis between the NIFTY-gridder algorithm and our improved NUFFT algorithm reveals that while the former gives higher accuracy and faster performance in wide-field imaging, our algorithm outperforms in scenarios without a wide field of view, despite increased computational time. Minor discrepancies notwithstanding, both algorithms demonstrate commendable performance.

Furthermore, for radio CME models involving both strong and weak sources, it is essential to consider the impact of CME location and strong sources on high-resolution imaging. The uniform circular array proves effective in observing CMEs when the intensity of both strong and weak sources is below 40 dB and not influenced by radio noise storms. Our study provides valuable insights into optimizing radioheliograph design for imaging radio CMEs, emphasizing the efficacy of our proposed improved NUFFT algorithms and the importance of accounting for CME location and source intensity in observational setups.

ACKNOWLEDGEMENTS

This research was supported by the grants of National Natural Science Foundation of China (42374219, 42127804) and the Qilu Young Researcher Project of Shandong University.

AUTHOR CONTRIBUTIONS

Weidan Zhang conceptualized and designed the solar radio imaging algorithm, and conducted experimental work. Weidan Zhang primarily drafted the original manuscript and provided the methodology. Bing Wang offered investigation support and conducted validation work. Bing Wang played a crucial role in data curation. Zhao Wu performed formal analysis, evaluating the effectiveness of the solar radio imaging algorithm. Yao Chen was responsible for data curation, ensuring the accuracy and consistency of the data. Fabao Yan reviewed and edited the manuscript, enhancing the overall quality. All authors read and approved the final manuscript.

DECLARATION OF INTERESTS

Yao Chen is an editorial board member for Astronomical Techniques and Instruments and was not involved in the editorial review or the decision to publish this article. The authors declare no competing interests.

REFERENCES

[1] Chhabra, S. 2021. Imaging spectroscopy of CME-associated solar radio bursts using OVRO-LWA. *The Astrophysical Journal*, **906**(2): 132.

[2] Tan, B. L. 2022. Diagnostic functions of solar coronal magnetic fields from radio observations. *Research in Astronomy and Astrophysics*, **22**(7): 13.

[3] Wang, W., Wang, L. H. 2023. Solar energetic electrons events. *Reviews of Geophysics and Planetary Physics*, **54**(4): 385−397. (in Chinese)

[4] Kansabanik, D. 2023. Deciphering radio emission from solar Coronal Mass Ejections using high-fidelity spectropolarimetric radio imaging. *arXiv:2310.16072*.

[5] Wagner, W. J. 1984. Coronal mass ejections. *Annual Review of Astronomy and Astrophysics*, **22**: 267−289.

[6] Illing, R. M. E., Hundhausen, A. J. 1985. Observation of a coronal transient from 1.2 to 6 solar radii. *Journal of Geophysical Research: Space Physics*, **90**(A1): 275−282.

[7] Forbes, T. G. 2000. A review on the genesis of coronal mass ejections. *Journal of Geophysical Research*, **105**(A10): 23153−23166.

[8] Webb, D. F., Howard, T. A. 2012. Coronal mass ejections: observations. *Living Reviews in Solar Physics*, **9**: 3.

[9] Carley, E. P., Vilmer, N., Vourlidas, A. 2020. Radio observations of coronal mass ejection initiation and development in the low solar corona. *Frontiers in Astronomy and Space Sciences*, **7**: 79.

[10] Ma, M. X., Shen, F., Liu, Y. S. 2022. Simulation study on the propagation process of coronal mass ejection. *Reviews of Geophysics and Planetary Physics*, **53**(4): 397−415.

[11] Thompson, A. R., Moran, J. M., Swenson, G. W. et al. 2017. Interferometry and synthesis in radio astronomy. 3rd Edition. Switzerland: Springer Cham.

[12] Pick, M. 1998. Joint Nancay radioheliograph and LASCO observations of coronal mass ejections – II, the 9 July 1996 event. *Solar Physics*, **181**(2): 455−468.

[13] Bastian, T. S., Pick, M., Kerdraon, A., et al. 2001. The coronal mass ejection of 1998 April 20: direct imaging at radio wavelengths. *The Astrophysical Journal*, **558**(1): L65−L69.

[14] Vourlidas, A., Carley, E. P., Vilmer, N. 2020. Radio observations of coronal mass ejections space weather aspects. *Frontiers in Astronomy and Space Sciences*, **7**: 43.

[15] Maia, D., Vourlidas, A., Pick, M., et al. 1999. Radio signatures of a fast coronal mass ejection development on November 6, 1997. *Journal of Geophysical Research*, **104**(A6): 12507−12514.

[16] Pohjolainen, S. 2001. On-the-disk development of the halo coronal mass ejection on 1998 May 2. *The Astrophysical Journal*, **556**(1): 421−431.

[17] Maia, D. J. F., Gama, R., Mercier, C., et al. 2007. The radio-coronal mass ejection event on 2001 April 15. *The Astrophysical Journal*, **660**(1): 874−881.

[18] Démoulin, P., Vourlidas, A., Pick, M., et al. 2012. Erratum: initiation and development of the white-light and radio coronal mass ejection on 2001 April 15. *The Astrophysical Journal*, **754**(2): 156.
[19] Yokoyama, T., Shibata, K. 1998. A two-dimensional magnetohydrodynamic simulation of chromospheric evaporation in a solar flare based on a magnetic reconnection model. *The Astrophysical Journal*, **494**(1): L113−L116.
[20] Grechnev, V. V. 2003. The siberian solar radio telescope: the current state of the instrument, observations, and data. *Solar Physics*, **216**(1): 239−272.
[21] Lonsdale, C. J. 2009. The murchison widefield array: design overview. *Proceedings of the IEEE* , **97**(8): 1497−1506.
[22] Yan, Y. H., Chen, L. J., Yu, S. J., et al. 2016. First radio burst imaging observation from Mingantu Ultrawide Spectral Radioheliograph. In Proceedings of the International Astronomical Union. **11**: 427−435.
[23] Wang, W., Yan, Y. H., Tan, B. L., et al. 2024. Wide-band solar radio spectral monitoring in the Phase II of Chinese Meridian Project. *Reviews of Geophysics and Planetary Physics*, **55**(1): 1−5. (in Chinese)
[24] Dewdney, P. E., Hall, P. J., Schilizzi, R. T., et al. 2009. The Square Kilometre Array. *IEEE Proceedings*, **97**(8): 1482−1496.
[25] Lu, G., Wang, B., Chen Y., et al. 2022. Simulations of the antenna-shielding effect of the Daocheng Solar Radio Telescope (DSRT). *Chinese Journal of Space Science*, **42**(2): 294−305. (in Chinese)
[26] Yan, J. Y., Wu, J., Wu, L., et al. 2023. A super radio camera with a one-kilometer lens. *Nature Astronomy*, **7**: 750.
[27] Lüdke, E., Sawant, H. S., Subramanian, K. R., et al. 2000. Solar imaging capabilities of the Brazilian Decimetric Array. *Geofísica International*, **39**(1): 147–152.
[28] Koshiishi, H., Enome, S., Nakajima, H., et al. 1994. Evaluation of the imaging performance of the Nobeyama radioheliograph. *Publications of the Astronomical Society of Japan*, **46**: L33–L36.
[29] Lanman, A. E., Kern, N., 2019. healvis: Radio interferometric visibility simulator based on HEALpix maps. Astrophysics Source Code Library. https://github.com/rasg-affiliates/healvis.
[30] Greisen, E. W. 2003. AIPS, the VLA, and the VLBA. In Information Handling in Astronomy-Historical Vistas. 285：109–125.
[31] McMullin, J. P., Waters, B., Schiebel, D., et al. 2007. CASA architecture and applications. In Astronomical Data Analysis Software and Systems XVI ASP Conference Series. **376**:127.
[32] Shepherd, M. C., Pearson, T. J., Taylor, G. B. 1994. DIFMAP: an interactive program for synthesis imaging. *Bulletin of the Astronomical Society*, **26**(2): 987–989.
[33] Perley, R. A., Chandler, C. J., Butler, B. J., et al. 2011. The expanded Very Large Array: a new telescope for new science. *The Astrophysical Journal Letters*, **739**: L1.
[34] Shimojo, M., Bastian, T. S., Hales, A. S., et al. 2017. Observing the Sun with the Atacama Large Millimeter/submillimeter Array (ALMA): high-resolution interferometric imaging. *Solar Physics*, **292**: 87.
[35] Barnett, A. H., Magland, J., af Klinteberg, L. 2019. A parallel nonuniform fast Fourier transform library based on an "Exponential of Semicircle" Kernel. *SIAM Journal on Scientific Computing*, **41**(5): C479−C504.
[36] Briggs, D. S., Schwab, F. R., Sramek, R. A. 1999. Synthesis imaging in Radio Astronomy II. In Astronomical Society of the Pacific Conference Series. **180**: 127−148.
[37] Li, S. S., Luo, K. D., Wei, S. L., et al. 2022. A distributed gridding implementation method for radio interferometric visibilities based on dask. *Astronomical Research & Technology*, **19**(1): 21−28. (in Chinese)
[38] Maia, D., Pick, M., Hawkins, S. E., et al. 2001. A near-global coronal event and its association with energetic electron events detected in the interplanetary medium. *Solar Physics*, **204**: 197−212.